tvst

DOI: 10.1167/tvst.5.2.6

Article

Correlating Photoreceptor Mosaic Structure to Clinical Findings in Stargardt Disease

Moataz M. Razeen[1,2], Robert F. Cooper[3], Christopher S. Langlo[4], Mara R. Goldberg[1], Melissa A. Wilk[4], Dennis P. Han[1], Thomas B. Connor, Jr.[1], Gerald A. Fishman[5,6], Frederick T. Collison[5], Yusufu N. Sulai[1], Alfredo Dubra[1,3,4,7], Joseph Carroll[1,3,4,7], and Kimberly E. Stepien[1]

[1] Department of Ophthalmology & Visual Sciences, Medical College of Wisconsin, Milwaukee, WI, USA
[2] Alexandria Faculty of Medicine, Alexandria University, Alexandria, Egypt
[3] Department of Biomedical Engineering, Marquette University, Milwaukee, WI, USA
[4] Department of Cell Biology, Neurobiology & Anatomy, Medical College of Wisconsin, Milwaukee, WI, USA
[5] The Pangere Center for Hereditary Retinal Diseases, the Chicago Lighthouse for People Who Are Blind or Visually Impaired, Chicago, IL, USA
[6] Department of Ophthalmology and Visual Sciences, University of Illinois at Chicago, Chicago, IL, USA
[7] Department of Biophysics, Medical College of Wisconsin, Milwaukee, WI, USA

Correspondence: Kimberly E. Stepien, Medical College of Wisconsin, Department of Ophthalmology, 925 N. 87th Street, Milwaukee, WI 53226, USA. e-mail: kstepien@mcw.edu

Received: 16 September 2015
Accepted: 6 January 2016
Published: 11 March 2016

Keywords: retina; imaging/image analysis; photoreceptors; Stargardt disease

Citation: Razeen MM, Cooper RF, Langlo CS, et al. Correlating photoreceptor mosaic structure to clinical findings in Stargardt disease. Trans Vis Sci Tech. 2016;5(2):6, doi:10.1167/tvst.5.2.6

Purpose: To demonstrate a method for correlating photoreceptor mosaic structure with optical coherence tomography (OCT) and microperimetry findings in patients with Stargardt disease.

Methods: A total of 14 patients with clinically diagnosed Stargardt disease were imaged using confocal and split-detection adaptive optics scanning light ophthalmoscopy. Cone photoreceptors were identified manually in a band along the temporal meridian. Resulting values were compared to a normative database ($n = 9$) to generate cone density deviation (CDD) maps. Manual measurement of outer nuclear layer plus Henle fiber layer (ONL+HFL) thickness was performed, in addition to determination of the presence of ellipsoid zone (EZ) and interdigitation zone (IZ) bands on OCT. These results, along with microperimetry data, were overlaid with the CDD maps.

Results: Wide variation in foveal structure and CDD maps was seen within this small group. Disruption of ONL+HFL and/or IZ band was seen in all patients, with EZ band preservation in regions with low cone density in 38% of locations analyzed. Normality of retinal lamellar structure on OCT corresponded with cone density and visual function at 50/78 locations analyzed. Outer retinal tubulations containing photoreceptor-like structures were observed in 3 patients.

Conclusions: The use of CDD color-coded maps enables direct comparison of cone mosaic local density with other measures of retinal structure and function. Larger normative datasets and improved tools for automation of image alignment are needed.

Translational Relevance: The approach described facilitates comparison of complex multimodal data sets from patients with inherited retinal degeneration, and can be expanded to incorporate other structural imaging or functional testing.

Introduction

Stargardt disease (STGD) is the most prevalent form of juvenile-onset macular dystrophy, with an estimated incidence of 1 in 10,000.[1] The most common form of STGD is autosomal recessive and is caused by mutations in the photoreceptor-specific *ABCA4* gene; responsible for coding an ATP-binding cassette transporter that is hypothesized to be involved in the clearance of a byproduct of the photoreceptor retinoid (Vitamin A) cycle from photoreceptors.[2,3] Disrupted clearance results in

premature accumulation of lipofuscin in retinal pigment epithelial (RPE) cells, which is a hallmark of the disease and is thought to lead to toxicity and eventual photoreceptor cell death. The disease presents in childhood in approximately 40% of patients with symptoms including central visual loss, impaired color discrimination, photoaversion, paracentral scotomas, and slow dark adaptation.[4] Fundus findings characteristically include yellow-white pisciform deposits (referred to as "fundus flecks") and atrophic-appearing macular lesions. Fundus flecks are caused by excessive accumulation of lipofuscin in the RPE which may be present before clinical symptoms. Diagnosis is based mainly on identifying these flecks and observing a dark choroid on fluorescein angiography.[5]

Near-infrared and short wavelength fundus autofluorescence, optical coherence tomography (OCT), and confocal adaptive optics scanning light ophthalmoscopy (AOSLO) have expanded our knowledge of STGD.[6–16] Subtypes of fundus autofluorescence lesions are used to predict disease progression[11,12] and characteristic structures visualized by OCT, including Bruch's membrane/RPE complex and choroidal hyperreflective foci, may be associated with disease severity.[17] Areas of abnormal findings on fundus autofluorescence and OCT in individuals with STGD have been shown to be correlated with disruptions of the cone photoreceptor mosaic on AOSLO.[14–16]

Although confocal AOSLO offers the ability to image the retina with cellular resolution, there are important limitations for its application in studying the degenerating retina. First, visualization of photoreceptor cells is thought to rely on normal photoreceptor waveguiding.[18–20] As such, it is challenging to discriminate between a cell with impaired waveguiding from one that has degenerated. In addition, cones in the diseased retina sometimes can have complex or "multi-modal" reflective profiles, making it difficult to differentiate reliably between rods and cones. The recently developed nonconfocal split-detection AOSLO[18] allows for enhanced visualization of the photoreceptor mosaic, enabling the visualization of inner segments even in the presence of disrupted outer segment structure. However, regardless of the AOSLO modality used, it often is challenging to put such high-resolution images into context with other structural and functional data from a given patient. We propose an approach for combining information about the photoreceptor mosaic with data from conventional clinical imaging and testing modalities, illustrated in patients with STGD.

Methods

Subjects

This study was approved by the Medical College of Wisconsin Institutional Review Board and adhered to the tenets of the Declaration of Helsinki. Patients with clinically diagnosed STGD provided written informed consent after the nature and potential risks of the procedure were explained. Exclusion criteria included patients with concurrent retinal disease, advanced cataract, corneal anomalies, or any other condition that would affect image acquisition quality. A total of 14 patients underwent comprehensive ophthalmic examination, genetic testing, fundus photography (Zeiss Visucam; Carl Zeiss Meditec, Dublin, CA), axial length measurements (Zeiss IOL Master; Carl Zeiss Meditec), microperimetry (Spectral OCT/SLO; OPKO/OTI, Miami, FL), OCT, and AOSLO imaging. The Gullstrand II schematic eye model was used, where the predicted 291 μm per degree of visual angle[21] was scaled linearly by the subject's axial length, to determine the scale of AOSLO and OCT imagery. Macular microperimetry was performed predilation after a brief training to allow for familiarization of the test. A 20° Crosshair grid composed of 40 points arranged in 4 meridians (10 points per each meridian; points being 2° apart) was performed using a Goldman III stimulus (approximately 0.4°), a 200 ms duration and a fast 2 dB test strategy. Pupils were dilated and cyclopleged using a combination of 2.5% phenylephrine hydrochloride solution (Bausch & Lomb Inc., Tampa, FL) and 1% tropicamide ophthalmic solution (Akorn Inc., Lake Forest, IL). One patient (KS_1027) was followed up 1 year after the initial visit.

Genetic Testing

Blood samples were drawn and DNA was isolated through one of several institutions (Edward S. Harkness Eye Institute, New York, NY; GeneDX, Gaithersburg, MD; Casey Eye Institute Molecular Diagnostics Laboratory, Oregon Health and Science University, Portland, OR; and CarverLab, University of Iowa, Iowa City, IA). The pathogenicity of nonsynonymous variations was predicted by PolyPhen-2[22] and Mutation Taster.[23] Synonymous variations were analyzed using RESCUE-ESE program[24] and intronic variations were analyzed with NetGene2

Table 1. Patient Demographics, Fixation Parameters and Genetic Results

Patient ID	Sex	Age	Eye	VA	Fixation		*ABCA4* Mutations[a]
					PRL	BCEA (arcmin^2)	
KS_1027[b,c]	F	53	OS	20/40	Central	4569	c.2160+1 G>T
TC_1048[b]	F	46	OS	20/25	Central	8176	c.2160+1 G>T
DH_1158	F	56	OD	20/20	Central	4293	c.4469 G>A; p. Cys1490Tyr
DH_1162	F	60	OD	20/40	Central	9109	c.2041 C>T; p. Arg681Stop
DH_10019	F	77	OS	20/50	Poor central	38,007	c.3259 G>A; p. Glu1087Lys
KS_10108[d]	F	15	OD	20/70	Poor central	15,339	c.1804 C>T; p. Arg602Trp c.2588 G>C; p. Gly863Ala
KS_10150	F	16	OS	20/20	Central	2027	c.1622 T>C; p. Leu541Pro c.3113 C>T; p. Ala1038Val c.5714+5 G>A
JC_10222	F	45	OD	20/20	Central	765	c.6079 C>T; p. Leu2027Phe c.6320 G>A; p. Arg2107His
KS_10241[e]	F	49	OD	20/20	Central	1728	c.1957 C>T; p. Arg653Cys
KS_10242[e]	F	25	OD	20/200	Eccentric	17,911	c.1957 C>T; p. Arg653Cys c.5882 G>A; p. Gly1961Glu
JC_10296	F	51	OD	20/60	Central	3240	c.5882 G>A; p. Gly1961Glu c.6449 G>A; p. Cys2150Tyr
KS_10306	F	23	OS	20/70	Central	14,853	c.676 C>T; p. Arg226Cys c.5018+8 A>G c.6730-579 T>C c.2919-927 T>A
JC_10461[f]	F	28	OS	20/25	Central	5259	c.4577 C>T; p. Thr1526Met c.5882 G>A; p. Gly1961Glu
JC_10469[f]	F	25	OD	20/32	Central	8202	c.4577 C>T; p. Thr1526Met c.5882 G>A; p. Gly1961Glu

F, female; OD, right eye; OS, left eye; VA, visual acuity; PRL, preferred retinal locus; BCEA, bivariate contour ellipse area.

[a] Only mutations previously reported, predicted/probably damaging, or of unknown significance are reported here. See Supplemental Table S1 for a complete list of *ABCA4* mutations. All mutations listed here are heterozygous. Genotyping was performed by Casey Eye Institute Molecular Diagnostics Laboratory (KS_10306, TC_1048, KS10241, KS_10242, KS_10150, JC_10296, JC_10461, JC_10469), GeneDX (DH_1162, KS_1027, DH_10019), CarverLab (DH_1158), and Edward S. Harkness Eye Institute (JC_10222).

[b] Sisters.

[c] Patient only evaluated for c.2160+1 G>T and c.5603 A>T mutations.

[d] Patient only evaluated for c.1804 C>T and c.2588 G>C mutations, as these were previously identified in her brother (not included in this study) through a more detailed genetic screening.

[e] Mother and daughter.

[f] Sisters.

server[25,26] and Human Splice Finder v3.0.[27] Of note, our population included two pairs of sisters and one mother-daughter pair (Table 1).

Optical Coherence Tomography

Optical coherence tomography (OCT) line and volume scans were acquired on all patients using Bioptigen SD-OCT (Bioptigen, Research Triangle Park, NC) and Cirrus HD-OCT (Carl Zeiss Meditec Inc.). The lateral scale of all OCT images was estimated by multiplying the nominal scan length with the ratio of the patient's axial length to that assumed by the instrument (24.00 mm for Bioptigen and 24.46 mm for Cirrus). Foveal center was determined using the Fovea Finder algorithm on the Cirrus OCT. Horizontal line scans (Bioptigen) were

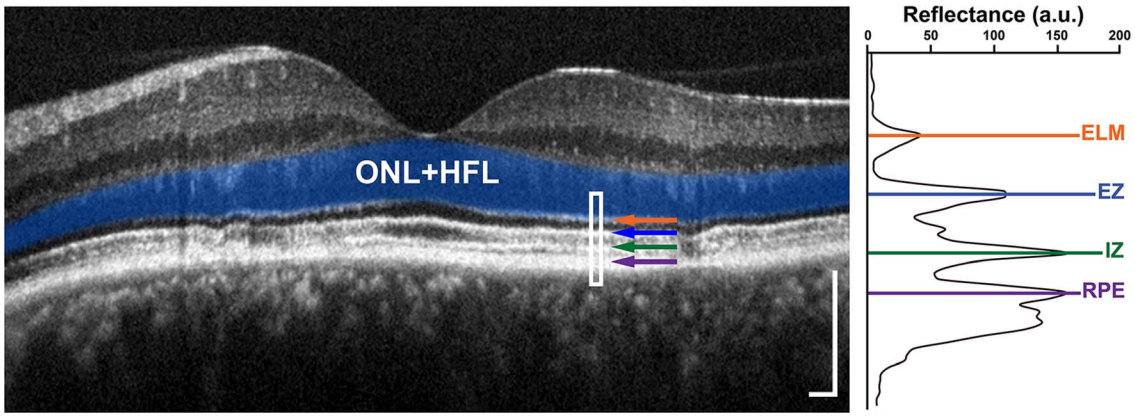

Figure 1. Representation of the analysis performed on OCT data. Logarithmic high-resolution horizontal line scan of the left eye of TC_1048. The manually segmented ONL/HFL complex is highlighted in *blue*. The *white rectangle* delineates an area of the OCT analyzed on the *right*. *Arrows* indicate the outer retinal hyperreflective bands as described previously: *orange*, ELM; *blue*, EZ; *green*, IZ; *purple*, RPE.[69] *Scale bars*: 200 μm. The *right* shows a longitudinal reflectivity profile analysis of the area enclosed by the *white rectangle* shown on the OCT scan using a previously described method.[29]

manually segmented to generate outer nuclear layer plus Henle fiber layer (ONL+HFL) thickness measurements at 0.1-mm intervals from the foveal center (Fig. 1). The data were compared to a normative database[28] and thresholded to areas either within or greater than 2 standard deviations (SDs) from the normal mean. The ONL+HFL analysis could be generated only up to 2.0 mm from the foveal center due to lack of normative data beyond that eccentricity. Longitudinal reflectivity profiles (LRPs) were generated from linear OCT images at the same locations to determine the presence/absence of the ellipsoid zone (EZ) and interdigitation zone (IZ) using a previously reported method[29] with a sampling window of 5 pixels. In areas of uncertainty, due to suboptimal image quality and/or severe pathology, they were generated using a narrower sampling window (1–3 pixels). Cirrus volume OCT scans (6 × 6 mm) were examined for presence of outer retinal tubulations. En face summed-volume projection images from the Bioptigen SD-OCT volumes for one patient (KS_1027) were generated to assess progression of outer retinal tubulations over time. These were derived using custom-designed software (Java; Oracle, Redwood City, CA) using a previously described method.[30]

AOSLO Image Acquisition and Processing

All patients underwent simultaneous confocal and split-detection imaging using a previously described AOSLO.[18,31] Image sequences were acquired over a 1.5° × 1.5° field of view, at 1.0° intervals from the foveal center out to 10° of visual angle temporal and superior to the fovea. Temporal strips were chosen to be used in data analysis to allow comparison to preexisting normative data along this meridian.[29] Superior strips were used to aid in registering AOSLO data onto fundus and OCT images. Image sequences were registered and averaged to create high signal-to-noise ratio images[32] that then were montaged manually using Adobe Photoshop CS6 (Adobe Systems, Inc., San Jose, CA). Microperimetry data, AOSLO montages and OCTs were appropriately scaled, then aligned manually and registered to fundus pictures using Adobe Photoshop CS6, using blood vessel patterns to aid in alignment.

Data Analysis

Quantitative analysis was restricted to 6° × 1° horizontal strips starting at 2° and extending out to 8° temporal to the foveal center. This was not possible in two patients due to a noncentral preferred retinal locus of fixation, causing montages to be offset from the absolute foveal center, and/or suboptimal image quality. Cone photoreceptors were identified manually in the cropped split-detection (Fig. 2A) and confocal horizontal strips, and data then were analyzed using custom MATLAB software (The Mathworks, Inc., Natick, MA). Cone density was calculated at each pixel using a 55 × 55 μm window to create a density map for each subject (Fig. 2B). Average cone density of a previously characterized normative population ($n = 9$; mean age ± SD = 25 ± 4.5 years; range = 20–35 years)[29] was used to fit an exponential function of density versus distance from the foveal center. For each subject, an eccentricity-

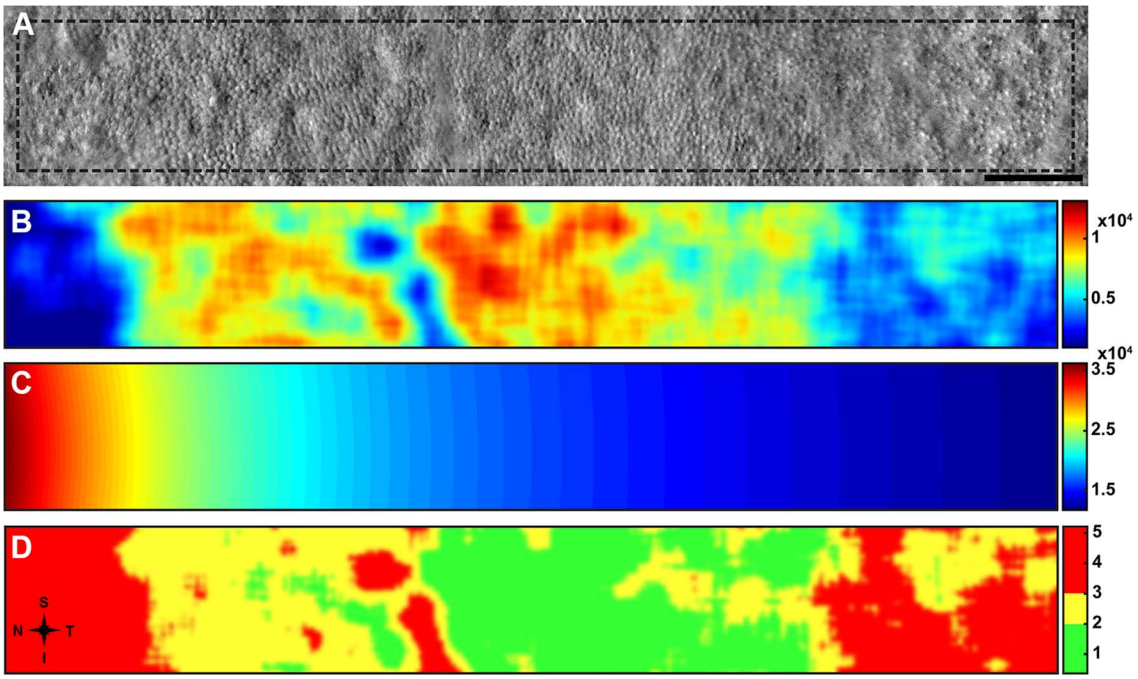

Figure 2. Generating a CDD map to highlight regional variation in cone density. (A) 6° x 1° split-detection montage strip of the right eye of KS_10108 extending from 2° (*left side*) to 8° (*right side*) temporal to the fovea. Area enclosed within the *dashed lines* represents the analyzed region. *Scale bar*: 300 μm. (B) Cone density map of KS_10108. (C) Normative mean cone density map ($n = 9$) starting 2° from foveal center. Unit of *color bars* in (B, C) *is cells/mm*^{2}. (D) Standard deviation map of KS_10108 showing regions with densities within 2 SDs (*green*), 3 SDs (*yellow*), and 4+ SDs (*red*) from normal mean. S, superior; N, nasal; T, temporal; and I, inferior.

and scale-matched normative density map was generated using this fit (Fig. 2C). The density at each pixel was compared to the corresponding location in the normative map and used to create a cone density deviation (CDD) map in SD units. This then was thresholded to highlight regions within 2, 3, and 4+ SDs from the normal mean (Fig. 2D).

Data from OCT were aligned according to distance from foveal center using Adobe Photoshop CS6. Locations of individual microperimetry data points then were marked on the AOSLO montage (after registration to the fundus picture) and then translated to the CDD map. Microperimtery data also were used to categorize patients' preferred foci of fixation into central, poor central, and eccentric (Table 1) using the classification scheme by Fujii et al.[33] Bivariate contour ellipse area (defined as retinal area in square minutes of arc in which the fixation point center would be found 68.3% of the time) was calculated for each patient from microperimetry data (Table 1) using a previously described method.[34] A 2-tailed Fisher's exact test was performed to examine the relation between different metrics. For two patients, the diameter of 50 arbitrarily selected rod inner segments, from split-detection images taken at 5° temporal retina, was measured manually using ImageJ.[35] The diameter of 50 RPE-like structures was quantified by the same method at the fovea in one patient.

Results

Demographics and Genetic Results

Patients ranged in age from 15 to 77 years with visual acuity ranging from 20/20 to 20/200 (demographics summarized in Table 1). Genetic analysis revealed 24 different mutations in the 14 patients. Despite the need for two or more mutations in the *ABCA4* gene to confirm the diagnosis of STGD, current data suggested that approximately 30% of individuals with a clinical diagnosis of an *ABCA4*-related disorder have only one identified mutation.[36,37] Excluding mutations predicted as likely benign, at least two mutations were found in eight patients (57%) and only one mutation was found in the remaining six patients (43%). To our knowledge, five of the 24 mutations have not been reported previously in the literature in relation to causing STGD (c.2160+1 G>T; c.676 C>T, p. Arg226Cys;

c.6730-579 T>C; c.2919-927 T>A; c.5018+8 A>G). The c.2160+1 G>T mutation also was not reported in the Single Nucleotide Polymorphism database[38] and thereby was considered a novel variant, though it occurs at a known site of mutation (previous report of c.2160+1 G>C[39]). The c.2160+1 G>T mutation is expected to destroy the canonical splice donor site in intron 14, thereby causing abnormal gene splicing and likely disease. The missense mutation c.676 C>T is predicted to be probably damaging. Two intronic variations (c.6730-579 T>C and c.2919-927 T>A) were predicted to possibly affect splicing due to alterations of splicing enhancers and silencers, though no conclusions can be made on the pathogenicity of these variants. The intronic variant c.5018+8 A>G was predicted to have no impact on splicing. Complete genetic results can be found in Table 1 and Supplemental Table S1.

Variable Foveal Structure in STGD

Foveal structure was highly variable within this small group as seen on OCT and split-detection AOSLO (Fig. 3 and Supplementary Figs. S1, S2). On OCT, transition zones between healthy and disrupted outer retinal structure were seen in four patients (KS_10241, KS_1027, DH_1158, and JC_10222). Irregular outer retinal disruption was noted in five patients (DH_1162, KS_10242, KS_10150, JC_10469, and DH_10019) and foveal atrophy, defined as complete loss of outer retinal structure, was seen in only one patient (JC_10296). On AOSLO, we observed an intact, contiguous foveal cone mosaic in seven of 14 patients, with visual acuity ranging from 20/20 to 20/70 in those patients. Six patients (DH_1162, KS_10242, KS_10150, JC_10469, KS_10108, and JC_10296) showed variable remnant foveal cone inner segment structure, with visual acuity ranging from 20/20 to 20/200. Patient DH_10019 (visual acuity = 20/50), in which irregular disruption was noted on OCT, had a mosaic of contiguous polygonal structures on split-detection and dark-field imaging (data not shown), averaging 19.6 ± 3.7 μm in diameter (range, 13.2–32.4 μm). The shape of these structures was consistent with normal RPE cell morphology,[40,41] despite being abnormal in size (Supplementary Fig. S2P). Similar RPE-like structures were seen in 5 additional patients (DH_1162, KS_10242: Figs. 3L, 3P; KS_10150, KS_10,108: Supplementary Figs. S1L, S1T; JC_10222: Supplementary Fig. S2K). In all but two patients, there was good correspondence between the integrity of the outer retinal hyperreflective bands (EZ/IZ) on OCT and the degree of remnant cone structure on AOSLO. In patient JC_10461, AOSLO showed rapid change in cone numerosity without a corresponding change in reflectivity of EZ/IZ bands on OCT (Figs. 3E–H). In addition, patches of remnant cone inner segments were observed in JC_10296 but no distinct EZ/IZ bands were seen on OCT (Supplementary Figs. S2Q–T).

Comparing Cone Structure on AOSLO and OCT Using CDD Map Overlays

In an effort to convey structural retinal changes relative to functional findings, CDD map overlays were created in 12 patients with good split-detection AOSLO montages of temporal retina and microperimetry data from the same locations. Corresponding ONL+HFL thickness and presence/absence of EZ and IZ bands are shown below each montage panel (Fig. 4 and Supplementary Fig. S3). The CDD maps showed regional variability of cone density in the parafovea of individual patients.

At least one area of the analyzed region in these 12 patients showed abnormally low cone density. The thickness of ONL+HFL was normal (within ± 2 SDs) across the whole analyzed region in only one patient (TC_1048). The ONL+HFL thickness and AOSLO cone density agreed at ≤2 SDs and ≤3 SDs (for analysis purposes) from normal mean respectively (both normal) or both fell out of defined normal limits (both abnormal). If only one measurement met defined normal parameters, disagreement between measurements was reported. The normality/abnormality of cone density used in deciding agreement/disagreement between different metrics was not limited to a certain area and was determined subjectively by two examiners who independently reviewed the data. For 81% of data points, ONL+HFL thickness status agreed with AOSLO cone density, with better agreement in areas of abnormality ($P = 0.0225$; Fisher's exact test). Areas where ONL+HFL was normal but cone density was abnormally low occurred in 14% of the data points, which might be expected due to the difference in lateral resolution between the two imaging modalities (AO and OCT). However, areas where the reverse occurred (5%), as shown in KS_10108 (Fig. 4), are most likely due to HFL (which constitutes up to 50% of the ONL+HFL thickness at this eccentricity and has normal topographical displacement)[42] thinning occurring as a result of the concurrent foveal outer retinal disruption (Supplementary Figs. S1Q–T).

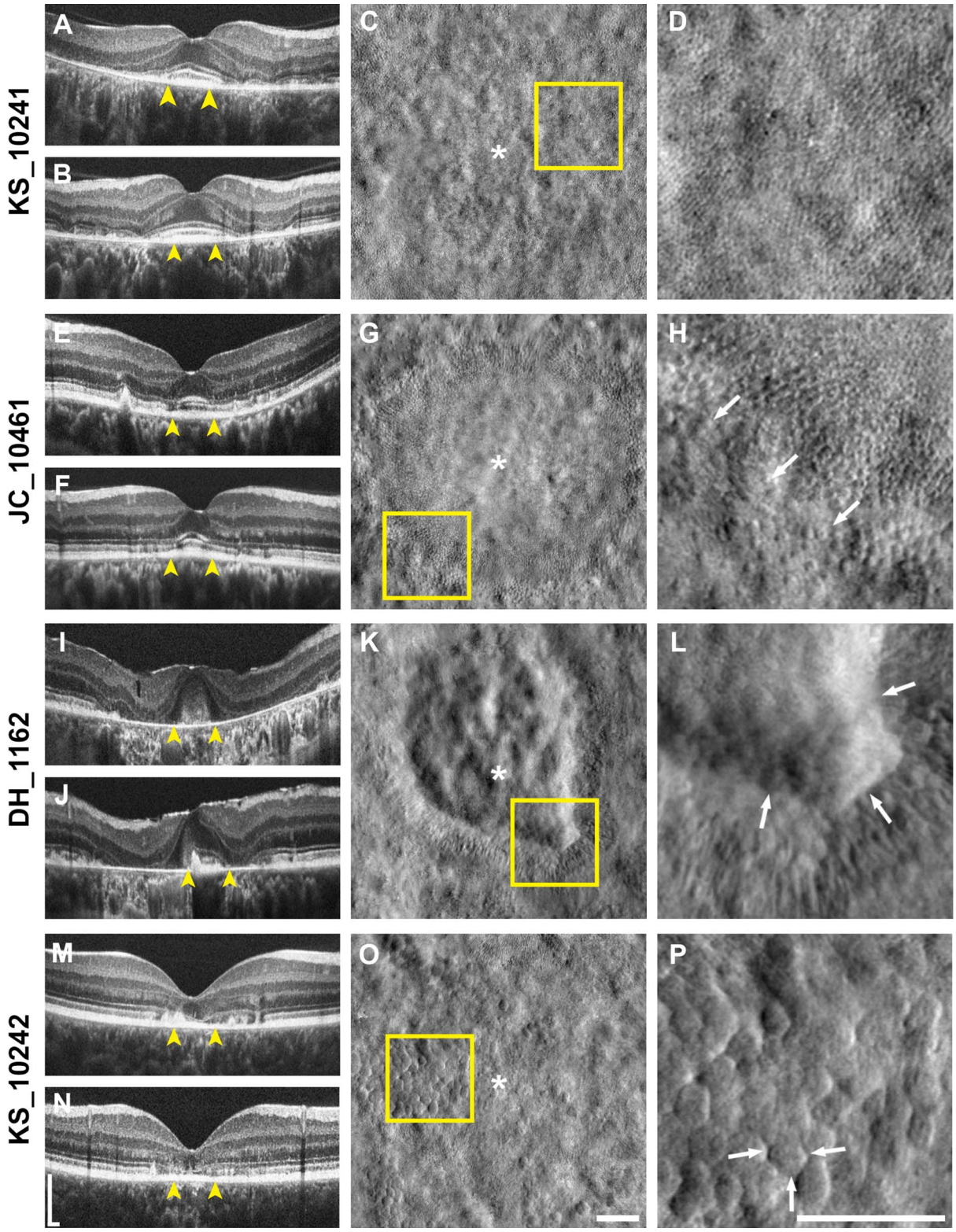

Figure 3. Spectrum of foveal structure. Horizontal (A, E, I, M) and vertical (B, F, J, N) OCT scans. *Arrowheads* denote the outer edges of the region imaged in (C, G, K, O). *Scale bar*: 200 μm. Split-detection montages centered on fixation (C, G, K, O) showing spectrum of foveal structure from intact foveal structure (C, G, K) to foveal atrophy (O). *Boxes* represent cropped images in column 3 and *asterisks* represent foveal center. (D, H, L, P) Images showing close to normal cone density (D), abrupt reduction in cone density ([H], *arrows*), a transition zone from retained foveal structure to atrophy ([L], *arrows*) and a region of polygonal structures hypothesized to be hypertrophied RPE cells ([P], *arrows* showing one cell). *Scale bar*: 100 μm. See Supplementary Figures S1 and S2 for additional panels.

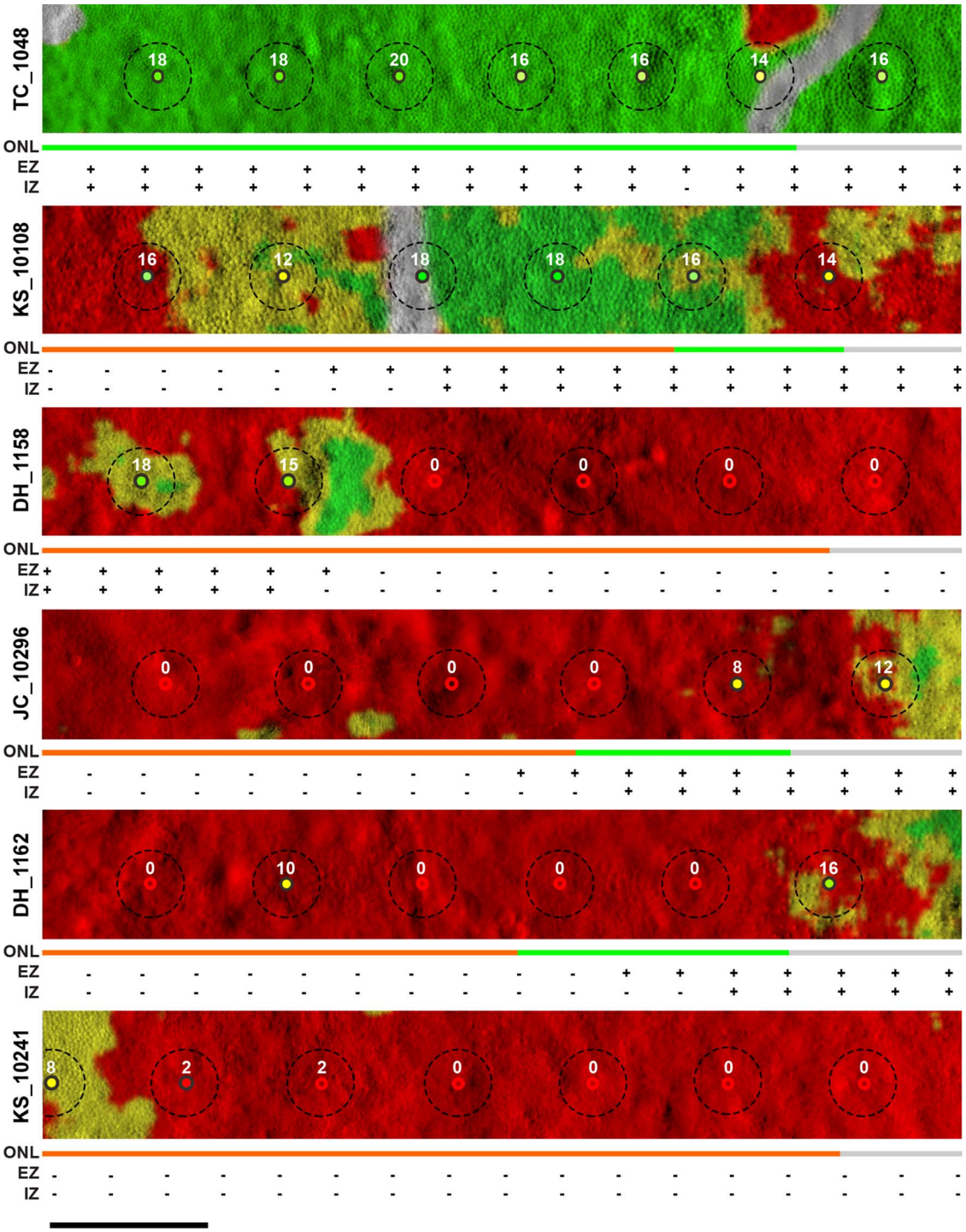

Figure 4. Cone density deviation map overlays on split-detection images combined with OCT and microperimetry data. Each panel consists of a CDD map overlaid on a split-detection montage and superimposed microperimetry data for one patient. ONL, EZ, and IZ data are displayed beneath each panel. All panels are shown as left eye equivalents extending from 2° (*left side*) to 8° (*right side*) temporal to the fovea. *Green*, *yellow*, *orange*, and *red* represent 2, 3, 3+, and 4+ SDs respectively, from normal mean for cone density and ONL thickness data. *Gray* represents unanalyzable data due to presence of blood vessels or unsatisfactory image quality (in *deviation map overlays*) and lack of normative data for comparison (in ONL analysis). +/− = present/absent. *Dashed circles* represent the area subtended by each microperimetry data point (reported in dB values in each circle). *Scale bar*: 1°. See Supplementary Figure S3 for additional panels.

According to LRP analysis findings, the IZ band was completely absent in six of 12 patients across the analyzed region, though it was disrupted by some degree in all patients. The integrity of the IZ band corresponded to cone density at 85% of locations measured (except JC_10461; Supplementary Fig. S3) with no statistically significant predilection to either normal or abnormal regions ($P = 1.0$; Fisher's exact test). In some instances (13%), the IZ remained intact in areas with abnormal cone density possibly due to nominal remnant cone structure (that is more than 4 SDs from mean). Conversely, the IZ was absent in areas with normal cone density at 2% of locations measured. As IZ band disruption has been reported in normals,[43] this metric may not necessarily be part of the disease process. However, due to the small number of patients studied and wide phenotypic variability, final conclusions from these observations could not be drawn.

The EZ band was completely absent, on LRP analysis, in only four of 12 patients, disrupted to some extent in five of 12, and present in the remaining three. Its integrity corresponded with cone density on AOSLO at only 62% of locations measured, and was more likely to agree in areas with normal cone density ($P < 0.0001$; Fisher's exact test). At remaining 38% of locations measured, the EZ was present despite abnormally low cone density. Preservation of EZ in these regions was likely due to the fact that rod photoreceptors contribute to this OCT band. Further examination of these areas, indeed, showed a contiguous mosaic of abnormally enlarged rod photoreceptors with dramatically reduced numbers of cone photoreceptors when compared to normal (Fig. 5). Typically, the diameter of a rod photoreceptor at a similar eccentricity to that in Figure 5 (5° temporal) is less than 3 μm[44–46]; however, in these patients, we observed larger values averaging 4.1 ± 0.5 μm (3.1–5.5 μm; range).

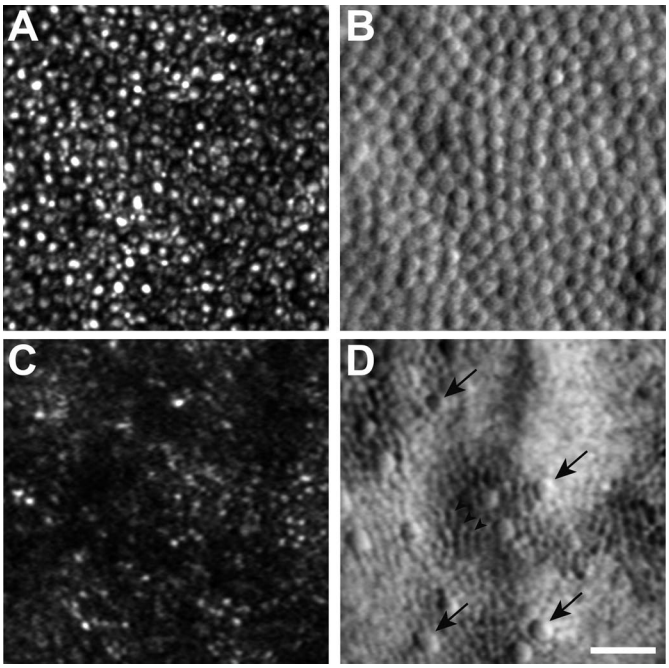

Figure 5. Rod structure in normal versus STGD. Confocal (A, C) and split-detection (B, D) images at 5° temporal to the fovea from a healthy control ([A, B], previously published)[18] and JC_10469 (C, D). *Arrows* represent cones and *arrowheads* (near the *center* of [D]) represent rods. Rods are seen in the split-detector images from this patient due to a reduced number of cones at this location and a concomitant increase in diameter compared to normal rods at the same retinal eccentricity, which are not visible due to resolution limits of split-detection.[18] At the location where C and D were obtained, IZ was absent, EZ was intact, ONL+HFL thickness and microperimetry were abnormal. *Scale bar*: 25 μm.

Comparing Retinal Structure and Function Using CDD Map Overlays

An additional feature afforded by the use of the CDD maps is the ability to compare retinal structure to function. All 12 patients had at least one abnormal (<15 dB) microperimetric location within the analyzed region. The normality of retinal layer structure on OCT and cone density corresponded with visual function at 50 of 78 locations analyzed (6–7 locations per patient; Fig. 4 and Supplementary Fig. S3), considering that each microperimetric retinal location tested subtended approximately 0.4°. Agreement was determined in areas of normal (within 2 SDs), subnormal (3 SDs), and abnormal (4+ SDs) cone density when microperimetry was normal (>15 dB),[47] subnormal (7–14 dB) and abnormal (0–6 dB), respectively. The OCT was considered normal, subnormal, or abnormal when at least two of the structures analyzed (ONL, EZ, IZ) were normal, subnormal, or abnormal, respectively. Locations with normal microperitmetry (>15 dB) were significantly more likely to show agreement among all three measurements (microperimetry, OCT, and AOSLO) than those with abnormal microperimetry ($P = 0.0255$; Fisher's exact test). Microperimetry coincided better with cone density alone; with agreement in 77 of 78 locations analyzed. This suggests that cone density may be a better predictor of visual function than OCT measures of ONL, EZ, or IZ integrity.

Outer Retinal Tubulations

Outer retinal tubulations in the central (6 × 6 mm) retina were found in three of 14 patients (~20%), in

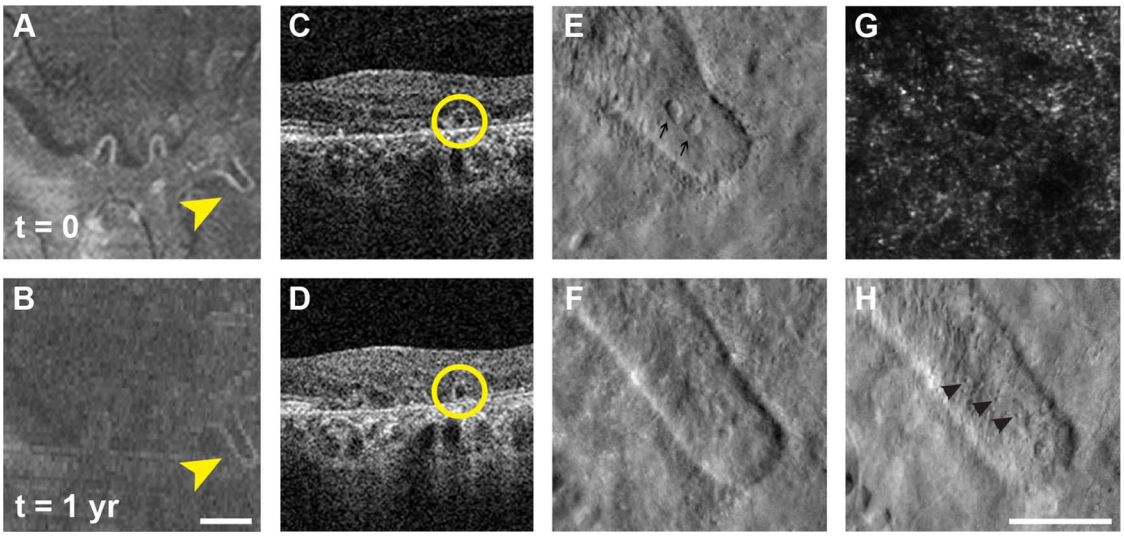

Figure 6. Outer retinal tubulation progression in KS_1027. (A, B) En face Bioptigen OCTs one year apart with *yellow arrowheads* pointing at the tubulation imaged with AOSLO. *Scale bar*: 300 μm. Horizontal Cirrus OCT line scans (C, D) showing a well circumscribed hyperreflective circular structure (*yellow circles*). Visual acuity was reduced from 20/30 to 20/40 over the same period of time. (E, F) Split-detection images showing enlargement and remodeling of the tubulation over time. Tear-drop like structures were clearly visible in E (*arrows*). (G) Corresponding confocal image of (E). (H) Split-detection image approximately 60 μm posterior to (F) revealing probable remains of photoreceptor structure (*black arrowheads*). *Scale bar*: 100 μm.

agreement with a previous report.[48] Figure 6 shows how these structures appear on confocal and split-detection AOSLO over a period of 1 year, during which the tubulation increased in length by approximately 30%. These tubulations were not clearly visualized on confocal AO imaging and appear as finger-like projections on the split-detection images. Characteristic tear-drop like structures were found in the center of these tubulations (Fig. 6E) and appeared to shrink in size over time. We hypothesize that these structures might be migratory RPE cells as it has been shown that RPE migration is common in end-stage retinal degenerations, with these cells becoming more spindle-shaped during repair and regeneration.[49] Deep (posterior) in the structure of the tubulation, AOSLO split-detection showed what is likely to be photoreceptor inner segment-like structures (Fig. 6H), consistent with histological findings.[50]

Discussion

In this study, we combined data from AOSLO, OCT, and microperimetry to create a method that conveys structure-function relationships in STGD. Using this technique, we were able to show wide variability in foveal structure across a small patient group ($n = 14$) supporting a hypothesis of multiple disease mechanisms.[51] Broad allelic heterogeneity also was recorded in this patient group as has been seen before in *ABCA4* retinopathies.[2,52–55] A particular case of interest was KS_10242 who, unlike her mother (KS_10241), presented with foveal atrophy with significant reduction in visual acuity (20/200 vs. 20/20) despite her younger age (Fig. 3). It may be that the additional genetic mutation she possesses (c.5882 G>A; p. Gly1961Glu) might be the cause of the different phenotypes exhibited in this family. Unfortunately, the phenotypic variability, genetic heterogeneity, and small sample size limited our ability to quantify genotype-phenotype correlations in more depth.[53,56]

As previously established,[57] severity of atrophic changes (accompanied with reduced cone density) in the fovea was not found to correspond to visual acuity in this patient group. We hypothesize that this may be due to patients acquiring eccentric fixation at a parafoveal location with viable structure.[58,59] We tested our hypothesis using the classification scheme by Fujii et al.,[33] by which the preferred retinal locus was found to be central in 11 patients, poor central in two patients, and eccentric in one patient. Moreover, bivariate contour ellipse area was abnormal in 13 of 14 patients (mean value 9534 arcmin^2; normal range from 80–1200 arcmin^2)[60] showing that fixation was largely unstable in this patient group, further supporting our hypothesis.

The CDD maps used here facilitated high-level interpretation of the AOSLO data. They proved to be sensitive to regional cone density variability and are a more accurate representation of actual structure than interpolating densities recorded from small regions of interest to larger retinal areas. When combined with microperimetry and OCT data, these maps showed regions of agreement and disagreement between the different imaging modalities. One source of disagreement might be attributable to inaccuracies from the use of regular microperimetry versus an AOSLO-based microperimety.[61] Another can originate from the inability of current OCT, unlike split-detection AOSLO, in distinguishing between rod and cone structure in areas of atrophy.

In this study we used split-detection AOSLO to follow outer retinal tubulations longitudinally, complementing previous studies using offset pinhole AOSLO,[62] OCT,[63–65] and histology.[50,66] Zweifel et al.[63] described outer retinal tubulations as circular/ovoid structures within the ONL with hyperreflective borders, resembling cystoid macular edema. These tubulations are believed to occur in response to RPE loss/dysfunction and occur more frequently in patients with intact foveal structure.[63,67] We found evidence of tubulations in three of 14 patients (~20%), all of whom presented with intact outer retinal foveal structure, consistent with those studies. Recently, Schaal et al.[66] showed that the hyperreflective borders of the tubulations are formed by the ELM and inner segment mitochondria, and that intralumenal hyperreflective material represents trapped RPE and non-RPE cells. One group of these non-RPE cells is the cone inner segments, which have been shown to survive for extended periods of time inside the tubulations.[65] These previous reports help support our hypothesis regarding the structures found at different depths of the tubulation shown in this study.

Limitations of this study included a small patient sample size (all with relatively good acuity), nonage-matched controls, and confounds in ONL measures (normative data limited to ±2 mm and inclusion of the HFL). Despite these limitations, the combined use of OCT, microperimetry, and CDD maps (generated using AOSLO) represents a potentially clinically useful method for visualizing structure-function relationships in patients with STGD. Future studies using this tool should allow for better understanding of disease status and pathophysiologic changes that occur with progression of STGD as well as other inherited retinal degenerations.

Acknowledgments

The authors acknowledge the work and help of Phyllis Summerfelt, Brian Higgins, and Erika Phillips in data collection and processing. The authors also thank Brandon Wilk for his help with the interpretation of genetics results. En face OCT software was developed by Robert Cooper and Michael Han implementing the segmentation algorithm developed by Chiu et al.[68]

Supported by the National Eye Institute, National Institutes of Health (NIH; Bethesda, MD) Grants T32EY014537, P30EY001931, and R01EY017607 and National Institute of General Medical Sciences, NIH Grants T32GM080202. This study was conducted in a facility constructed with support from the National Center for Research Resources, NIH (C06RR016511). Additional support was provided by Thomas M. Aaberg, Sr., Retina Research Fund, Foundation Fighting Blindness, Pangere Family Foundation, Thome Memorial Foundation and a Career Development Award to A. Dubra from Research to Prevent Blindness. The authors alone are responsible for the content and writing of this paper.

Disclosure: **M.M. Razeen**, None; **R.F. Cooper**, None; **C.S. Langlo**, None; **M.R. Goldberg**, None; **M.A. Wilk**, None; **D.P. Han**, None; **T.B. Connor, Jr.**, None; **G.A. Fishman**, None; **F.T. Collison**, None; **Y.N. Sulai**, None; **A. Dubra**, None; **J. Carroll**, None; **K.E. Stepien**, None

References

1. Blacharski PA, Newsome DA. Bilateral macular holes after nd: Yag laser posterior capsulotomy. *Am J Ophthalmol*. 1988;105:417–418.
2. Allikmets R, Singh N, Sun H, et al. A photoreceptor cell-specific ATP-binding transporter gene (*ABCR*) is mutated in recessive Stargardt macular dystrophy. *Nat Genet*. 1997;15:236–246.
3. Zhang K, Kniazeva M, Han M, et al. A 5-bp deletion in *ELOVL4* is associated with two related forms of autosomal dominant macular dystrophy. *Nat Genet*. 2001;27:89–93.
4. Rotenstreich Y, Fishman GA, Anderson RJ. Visual acuity loss and clinical observations in a

large series of patients with Stargardt disease. *Ophthalmology*. 2003;110:1151–1158.
5. Lambertus S, van Huet RA, Bax NM, et al. Early-onset Stargardt disease: phenotypic and genotypic characteristics. *Ophthalmology*. 2015; 122:335–344.
6. Song H, Rossi EA, Latchney L, et al. Cone and rod loss in Stargardt disease revealed by adaptive optics scanning light ophthalmoscopy. *JAMA Ophthalmol*. 2015;133:1198–203.
7. Ergun E, Hermann B, Wirtitsch M, et al. Assessment of central visual function in Stargardt's disease/fundus flavimaculatus with ultra-high-resolution optical coherence tomography. *Invest Ophthalmol Vis Sci*. 2005;46:310–316.
8. Gomes NL, Greenstein VC, Carlson JN, et al. A comparison of fundus autofluorescence and retinal structure in patients with Stargardt disease. *Invest Ophthalmol Vis Sci*. 2009;50:3953–3959.
9. Greenstein VC, Schuman AD, Lee W, et al. Near-infrared autofluorescence: its relationship to short-wavelength autofluorescence and optical coherence tomography in recessive Stargardt disease. *Invest Ophthalmol Vis Sci*. 2015;56: 3226–3234.
10. Duncker T, Lee W, Tsang SH, et al. Distinct characteristics of inferonasal fundus autofluorescence patterns in Stargardt disease and retinitis pigmentosa. *Invest Ophthalmol Vis Sci*. 2013;54: 6820–6826.
11. Fujinami K, Zernant J, Chana RK, et al. Clinical and molecular characteristics of childhood-onset Stargardt disease. *Ophthalmology*. 2015;122:326–334.
12. Parodi MB, Iacono P, Triolo G, et al. Morpho-functional correlation of fundus autofluorescence in Stargardt disease. *Br J Ophthalmol*. 2015;99: 1354–1359.
13. Huang WC, Cideciyan AV, Roman AJ, et al. Inner and outer retinal changes in retinal degenerations associated with *ABCA4* mutations. *Invest Ophthalmol Vis Sci*. 2014;55:1810–1822.
14. Chen YF, Roorda A, Duncan JL. Advances in imaging of Stargardt disease. *Adv Exp Med Biol*. 2010;66:333–340.
15. Chen Y, Ratnam K, Sundquist SM, et al. Cone photoreceptor abnormalities correlate with vision loss in patients with Stargardt disease. *Invest Ophthalmol Vis Sci*. 2011;52:3281–3292.
16. Pang CE, Suqin Y, Sherman J, Freund KB. New insights into Stargardt disease with multimodal imaging. *Ophthalmic Surg Lasers Imaging Retina*. 2015;46:257–261.
17. Piri N, Nesmith BL, Schaal S. Choroidal hyper-reflective foci in Stargardt disease shown by spectral-domain optical coherence tomography imaging: correlation with disease severity. *JAMA Ophthalmol*. 2015;133:398–405.
18. Scoles D, Sulai YN, Langlo CS, et al. In vivo imaging of human cone photoreceptor inner segments. *Invest Ophthalmol Vis Sci*. 2014;55: 4244–4251.
19. Roorda A, Williams DR. Optical fiber properties of individual human cones. *J Vis*. 2002;25:404–412.
20. Enoch JM. Optical properties of the retinal receptors. *J Opt Soc Am*. 1963;53:71–85.
21. Hirsch J, Curcio CA. The spatial resolution capacity of human foveal retina. *Vision Res*. 1989;29:1095–1102.
22. Adzhubei I, Jordan DM, Sunyaev SR. Predicting functional effect of human missense mutations using PolyPhen-2. *Curr Protoc Hum Genet*. 2013; Chapter 7:Unit7 20.
23. Schwarz JM, Cooper DN, Schuelke M, Seelow D. MutationTaster2: mutation prediction for the deep-sequencing age. *Nat Methods*. 2014;11:361–362.
24. Fairbrother WG, Yeh RF, Sharp PA, Burge CB. Predictive identification of exonic splicing enhancers in human genes. *Science*. 2002;29:1007–1013.
25. Brunak S, Engelbrecht J, Knudsen S. Prediction of human mRNA donor and acceptor sites from the DNA sequence. *J Mol Bio*. 1991;220:49–65.
26. Hebsgaard SM, Korning PG, Tolstrup N, et al. Splice site prediction in Arabidopsis thaliana pre-mRNA by combining local and global sequence information. *Nucleic Acids Res*. 1996;241:3439–3452.
27. Desmet FO, Hamroun D, Lalande M, et al. Human splicing finder: an online bioinformatics tool to predict splicing signals. *Nucleic Acids Res*. 2009;37:e67.
28. Carroll J, Dubra A, Gardner JC, et al. The effect of cone opsin mutations on retinal structure and the integrity of the photoreceptor mosaic. *Invest Ophthalmol Vis Sci*. 2012;53:8006–8015.
29. Wilk MA, McAllister JT, Cooper RF, et al. Relationship between foveal cone specialization and pit morphology in albinism. *Invest Ophthalmol Vis Sci*. 2014;55:4186–4198.
30. Flatter JA, Cooper RF, Dubow MJ, et al. Outer retinal structure after closed-globe blunt ocular trauma. *Retina*. 2014;34:2133–2146.
31. Dubra A, Sulai Y. Reflective afocal broadband adaptive optics scanning ophthalmoscope. *Biomed Opt Express*. 2011;2:1757–1768.

32. Dubra A, Harvey Z. Registration of 2d images from fast scanning ophthalmic instruments. In: Fischer B, Dawant B, Lorenz C, eds. *Biomedical Image Registration*. Berlin: Springer; 2010:60–71.
33. Fujii GY, de Juan E Jr, Sunness J, et al. Patient selection for macular translocation surgery using the scanning laser ophthalmoscope. *Ophthalmology*. 2002;109:1737–1744.
34. Steinman RM. Effect of target size, luminance, and color on monocular fixation. *J Opt Soc Am*. 1965;55:1158–1165.
35. Schneider CA, Rasband WS, Eliceiri KW. NIH image to ImageJ: 25 years of image analysis. *Nat Methods*. 2012;9:671–675.
36. Briggs CE, Rucinski D, Rosenfeld PJ, et al. Mutations in *ABCR* (*ABCA4*) in patients with Stargardt macular degeneration or cone-rod degeneration. *Invest Ophthalmol Vis Sci*. 2001; 42:2229–2236.
37. Yatsenko AN, Shroyer NF, Lewis RA, Lupski JR. Late-onset Stargardt disease is associated with missense mutations that map outside known functional regions of *ABCR* (*ABCA4*). *Hum Genet*. 2001;108:346–355.
38. Sherry ST, Ward MH, Kholodov M, et al. DbSNP: the NCBI database of genetic variation. *Nucleic Acids Res*. 2001;29:308–311.
39. Lewis RA, Shroyer NF, Singh N, et al. Genotype/phenotype analysis of a photoreceptor-specific ATP-binding cassette transporter gene, *ABCR*, in Stargardt disease. *Am J Hum Genet*. 1999;64:422–434.
40. Ts'o MO, Friedman E. The retinal pigment epithelium. I. Comparative histology. *Arch Ophthalmol*. 1967;78:641–649.
41. Scoles D, Sulai YN, Dubra A. In vivo dark-field imaging of the retinal pigment epithelium cell mosaic. *Biomed Opt Express*. 2013;4:1710–1723.
42. Lujan BJ, Roorda A, Croskrey JA, et al. Directional optical coherence tomography provides accurate outer nuclear layer and Henle fiber layer measurements. *Retina*. 2015;35:1511–1520.
43. Park JC, Collison FT, Fishman GA, et al. Objective analysis of hyperreflective outer retinal bands imaged by optical coherence tomography in patients with Stargardt disease. *Invest Ophthalmol Vis Sci*. 2015;56:4662–4667.
44. Curcio CA, Sloan KR, Kalina RE, Hendrickson AE. Human photoreceptor topography. *J Comp Neurol*. 1990;292:497–523.
45. Curcio CA, Millican CL, Allen KA, Kalina RE. Aging of the human photoreceptor mosaic: evidence for selective vulnerability of rods in central retina. *Invest Ophthalmol Vis Sci*. 1993;34: 3278–3296.
46. Jonas JB, Schneider U, Naumann GOH. Count and density of human retinal photoreceptors. *Graefes Arch Clin Exp Ophthalmol*. 1992;230:505–510.
47. Takeuchi M, Iwasaki T, Kezuka T, et al. Functional and morphological changes in the eyes of Behcet's patients with uveitis. *Acta Ophthalmologica*. 2010;88:257–262.
48. Goldberg NR, Greenberg JP, Laud K, Tsang S, Freund KB. Outer retinal tubulation in degenerative retinal disorders. *Retina*. 2013;33:1871–1876.
49. Grierson I, Hiscott P, Hogg P, et al. Development, repair and regeneration of the retinal pigment epithelium. *Eye (Lond)*. 1994;8:255–262.
50. Curcio CA, Medeiros NE, Millican CL. Photoreceptor loss in age-related macular degeneration. *Invest Ophthalmol Vis Sci*. 1996;37:1236–1249.
51. Fujinami K, Sergouniotis PI, Davidson AE, et al. Clinical and molecular analysis of Stargardt disease with preserved foveal structure and function. *Am J Ophthalmol*. 2013;156:487–501.
52. Michaelides M, Hunt DM, Moore AT. The genetics of inherited macular dystrophies. *J Med Genet*. 2003;40:641–650.
53. Burke TR, Tsang SH. Allelic and phenotypic heterogeneity in *ABCA4* mutations. *Ophthalmic Genet*. 2011;32:165–174.
54. Fishman GA, Stone EM, Grover S, et al. Variation of clinical expression in patients with Stargardt dystrophy and sequence variations in the *ABCR* gene. *Arch Ophthalmol*. 1999;117:504–510.
55. Fujinami K, Akahori M, Fukui M, et al. Stargardt disease with preserved central vision: identification of a putative novel mutation in ATP-binding cassette transporter gene. *Acta Ophthalmol*. 2011;89:e297–298.
56. Aguirre-Lamban J, Gonzalez-Aguilera JJ, Riveiro-Alvarez R, et al. Further associations between mutations and polymorphisms in the *ABCA4* gene: clinical implication of allelic variants and their role as protector/risk factors. *Invest Ophthalmol Vis Sci*. 2011;52:6206–6212.
57. Ratnam K, Carroll J, Porco TC, Duncan JL, Roorda A. Relationship between foveal cone structure and clinical measures of visual function in patients with inherited retinal degenerations. *Invest Ophthalmol Vis Sci*. 2013;54:5836–5847.
58. Greenstein VC, Santos RA, Tsang SH, et al. Preferred retinal locus in macular disease: char-

acteristics and clinical implications. *Retina*. 2008; 28:1234–1240.
59. Sullivan B, Jovancevic-Misic J, Hayhoe M, Sterns G. Use of multiple preferred retinal loci in Stargardt's disease during natural tasks: a case study. *Ophthalmic Physiol Opt*. 2008;28:168–177.
60. Gonzalez EG, Teichman J, Lillakas L, Markowitz SN, Steinbach MJ. Fixation stability using radial gratings in patients with age-related macular degeneration. *Can J Ophthalmol*. 2006;41: 333–339.
61. Tuten WS, Tiruveedhula P, Roorda A. Adaptive optics scanning laser ophthalmoscope-based microperimetry. *Optom Vis Sci*. 2012;89:563–574.
62. King B, Sapoznik K, Elsner AE, Gast T, Burns SA. Outer retinal tubulation observed with SDOCT and AOSLO. *Invest Ophthalmol Vis Sci*. 2014;55:3401–3401.
63. Zweifel SA, Engelbert M, Laud K, et al. Outer retinal tubulation: a novel optical coherence tomography finding. *Arch Ophthalmol*. 2009;127: 1596–1602.
64. Hua R, Liu L, Hu Y, Chen L. The occurrence and progression of outer retinal tubulation in Chinese patients after intravitreal injections of Ranibizumab. *Sci Rep*. 2015;5:7661.
65. Jung JJ, Freund KB. Long-term follow-up of outer retinal tubulation documented by eye-tracked and en face spectral-domain optical coherence tomography. *Arch Ophthalmol*. 2012; 130:1618–1619.
66. Schaal KB, Freund KB, Litts KM, et al. Outer retinal tubulation in advanced age-related macular degeneration: optical coherence tomographic findings correspond to histology. *Retina*. 2015;35: 1339–1350.
67. Sergouniotis PI, Davidson AE, Lenassi E, et al. Retinal structure, function, and molecular pathologic features in gyrate atrophy. *Ophthalmology*. 2012;119:596–605.
68. Chiu SJ, Li XT, Nicholas P, et al. Automatic segmentation of seven retinal layers in SDOCT images congruent with expert manual segmentation. *Opt Express*. 2010;181:19413–19428.
69. Spaide RF, Curcio CA. Anatomical correlates to the bands seen in the outer retina by optical coherence tomography: literature review and model. *Retina*. 2011;31:1609–1619.